Materials Chemistry and Physics 210 (2018) 309–314

Contents lists available at ScienceDirect

Materials Chemistry and Physics

journal homepage: www.elsevier.com/locate/matchemphys

Elastic stability and lattice distortion of refractory high entropy alloys

Bojun Feng, Michael Widom*

Department of Physics, Carnegie Mellon University, Pittsburgh, PA 15213, USA

HIGHLIGHTS

- Simulated four High Entropy Alloy structures and comparison of pair correlation function.
- Elasticity of High Entropy Alloys.
- Comparison of static atomic displacements of High Entropy Alloys between simulated and theoretical values.
- Comparison of thermal atomic displacements of High Entropy Alloys between simulated and theoretical values.

ARTICLE INFO

Article history:
Received 11 March 2017
Received in revised form
24 May 2017
Accepted 17 June 2017
Available online 20 June 2017

2017 MSC:
00-01
99-00

Keywords:
High entropy alloy
Shear instability
Lattice distortion
Elastic stability

ABSTRACT

Refractory high entropy alloys containing elements from the Ti, V and Cr columns of the periodic table form body centered cubic (BCC) structures. Elements from the Ti column are noteworthy because they take the BCC structure at high temperature but undergo a shear instability and transform to the hexagonal (HCP) structure at low temperature. We show that the instability of these elements impacts the properties of the HEAs that contain them. In particular, the shear moduli are greatly reduced, causing increased dynamic contributions to lattice distortion. Relatively large size differences between elements of the BCC/HCP column compared with the regular BCC columns create additional static contributions to lattice distortion. These findings are supported by direct evaluation of elastic constants and lattice distortion in four representative HEAs. Comparing moduli of HEAs with those of compositionally averaged pure elements verifies the impact of BCC/HCP elements and allows us to estimate the compositions at which the BCC phases become elastically unstable, and these predictions could be useful in material design.

1. Refractory high entropy alloys

Many high entropy alloys (HEAs [1,2]) contain the refractory elements found in columns 2-4 of the transition metal series in the periodic table [3–5]. Elements in columns 3 and 4 (those starting with V and Cr, respectively) take a body centered cubic (BCC) structure at all temperatures below melting. In contrast, those in column 2 (starting with Ti) are BCC at high temperature but transform to hexagonal (HCP) at low temperature through a diffusionless “martensitic” transformation known as the Burgers distortion [6]. We refer to these as BCC/HCP elements. The refractory high entropy alloys, even those containing BCC/HCP elements, form BCC structures as-cast, and have not so far exhibited BCC to HCP transitions at lower temperatures.

The Burgers distortion begins with an orthorhombic shear deformation of the BCC structure [7]. The distortion breaks the symmetry, splits the metal *d*-orbitals and reduces the Fermi level density of states, hence lowering the total energy. To assess stability against this distortion we consider the elastic moduli of these elements and their alloys. Cubic structures have three independent elastic constants, C_{11}, C_{12} and C_{44} in Voigt notation; there are correspondingly three conditions of elastic stability, the Born rules [8]. The BCC/HCP elements violate these stability conditions at low temperatures, and they are stabilized at high temperatures through anharmonic vibrational entropy.

We will explore four representative refractory equimolar HEAs comprised of elements drawn from overlapping squares [9] of the periodic table. Two of the squares cover the Ti and V columns, and hence contain both BCC/HCP and regular BCC elements. The other two squares cover the V and Cr columns and hence contain only regular BCC elements. Fig. 1 illustrates representative structures within 128-atom cells simulated at $T = 1200$ K using hybrid Monte

* Corresponding author.
E-mail address: widom@andrew.cmu.edu (M. Widom).

http://dx.doi.org/10.1016/j.matchemphys.2017.06.038
0254-0584/

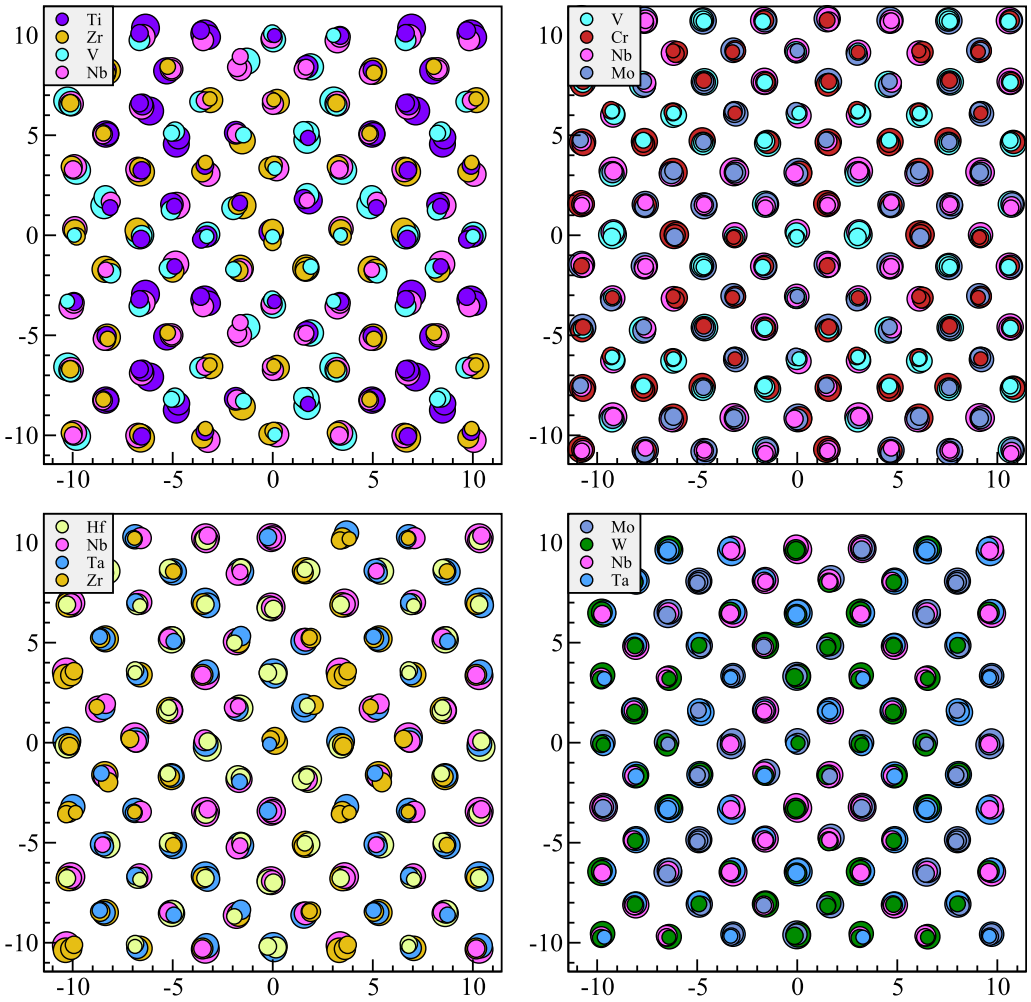

Fig. 1. Refractory HEA configurations at $T = 300$ K (quenched from 1200 K). Atomic species are color coded. Size indicates vertical height. NbTiVZr and HfNbTaZr contain both BCC/HCP and regular BCC elements, while CrMoNbV and MoNbTaW contain only regular BCC elements. (For interpretation of the references to colour in this figure legend, the reader is referred to the web version of this article.)

Carlo/molecular dynamics [10], then quenched to room temperature $T = 300$ K using conventional MD, so as to preserve the chemical order characteristic of high temperature. Displacements of atoms off their ideal sites are clearly visible, especially in the alloy systems containing BCC/HCP elements.

Pair correlation functions provide an alternate representation of the HEA structure. Fig. 2 presents partial pair correlation functions, separated into nearest neighbors (NN) and next nearest neighbors (NNN). The separation is achieved by defining pairs along the [111] direction as nearest neighbors and along [100] as next nearest. Rather than display all ten partials [9], $g_{\alpha\beta}$, for each alloy system, we group them into three classes according to which columns of the periodic table are represented; L and R indicate the left-hand and right-hand columns respectively. Several trends are evident. In all cases the NN correlations occur at larger distances for L-L than L-R with R-R being shortest, in keeping with the periodic table trend of decreasing atomic radius from left to right within each transition metal row. NN and NNN peaks overlap considerably for the two compounds containing BCC/HCP elements, and the overlaps are greatest for the L-L correlations which are specifically those of the BCC/HCP elements. In fact, summing the NN and NNN correlations, no separation can be observed between the NN and NNN peaks in these partials, as has been separately noted in the case of NbTiVZr [9]. Such effects have been reported experimentally in the medium entropy alloy HfNbZr [11].

2. Elasticity

We calculate elastic constants from stress-strain relationships of the two-atom BCC unit cells using numerical two point central differences as implemented in VASP [12] in the generalized gradient approximation [13]. Energy cutoffs of the plane wave basis sets are increased to 400 eV and k-point densities are increased to $3 \times 3 \times 3$ to achieve convergence of 1 GPa on all elastic constants. Elemental Cr is treated as an antiferromagnet. Because atomic coordinates and lattice constants are fully relaxed, elastic moduli are predicted for $T = 0$ K.

For all structures, we report the elastic moduli C_{ij} and also the Hill average [14] of the Voigt [15] and Reuss [16] polycrystalline moduli. For cubic materials these are [17].

$$K_V = K_R = K_H = \frac{1}{3}(C_{11} + 2C_{12}) \tag{1}$$

and

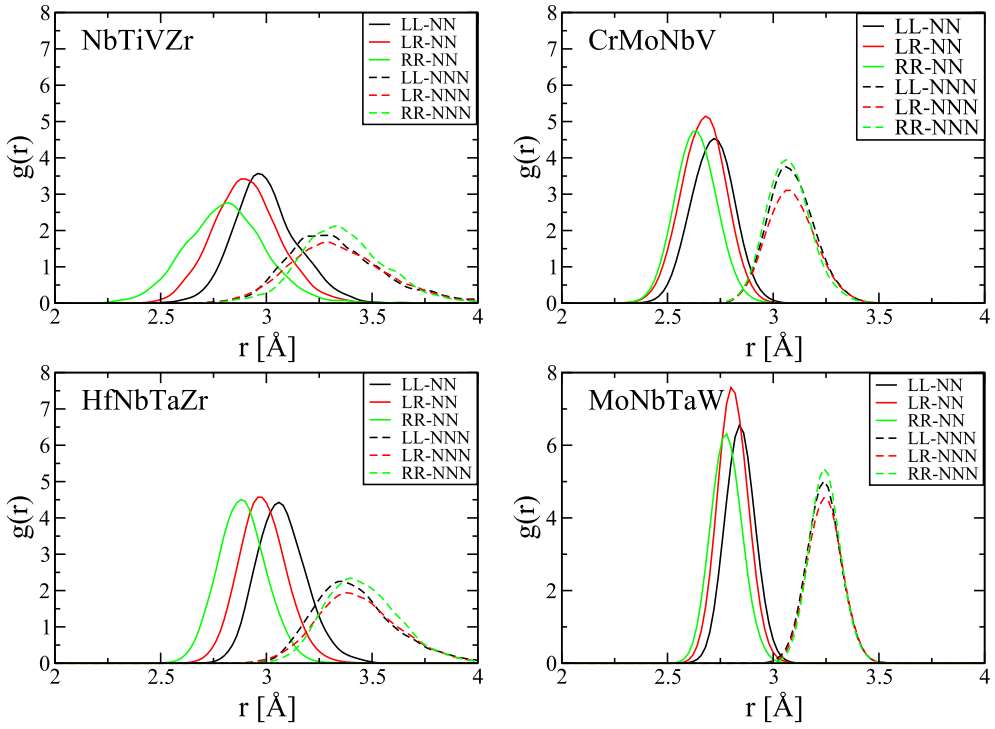

Fig. 2. Partial pair correlation functions averaged over molecular dynamics simulation at $T = 300$ K. L-L takes elements only from the left-hand periodic table column, L-R are correlations of left-hand and right-hand elements and R-R takes only right-hand elements. For example in NbTiVZr, L-L includes Ti-Ti, Ti-Zr, Zr-Ti and Zr-Zr pairs, while L-R includes Ti-Nb, Ti-V, Zr-Nb and Zr-V, etc. Solid lines are nearest neighbors (NN); dashed are next nearest neighbors (NNN).

$$G_V = \frac{1}{5}(C_{11} - C_{12} + C_{44}),\quad G_R = \frac{5(C_{11} - C_{12})C_{44}}{3C_{11} - 3C_{12} + 4C_{44}},\quad G_H = (G_V + G_R)/2. \tag{2}$$

We also report the Poisson ratio

$$\sigma = (3K_H - 2G_H)/(6K_H + 2G_H) \tag{3}$$

and also the Zener anisotropy [18] (ratio of shear moduli)

$$A_A = C_{44}/\mu = 2C_{44}/(C_{11} - C_{12}) \tag{4}$$

for which $A = 1$ indicates isotropy. In Eq. (4) we have defined the shear moduli as C_{44} and

$$\mu \equiv (C_{11} - C_{12})/2. \tag{5}$$

Born rules for stability [8] require positivity of the bulk modulus K_H and the two shear moduli, C_{44} and μ. These, in turn, imply bounds on the Poisson ratio $-1 < \sigma < 1/2$, and positivity of the anisotropy $A_Z > 0$.

Table 1 presents our results for pure elements of the transition metal columns 2-4 (starting with Ti, V and Cr). Vales of C_{11} and C_{12} lie within 20% of experimentally reported values in all cases, while values of the small C_{44} differ by up to a factor of 2. Notice the stability violations for BCC structures of the Ti column, verifying their shear instabilities ($\mu < 0$) at low temperature. Moduli and elastic stabilities increase, and Poisson ratios decrease, from left to right in the periodic table as nuclear charges and chemical bonding strength increase, and atomic volumes drop.

Moduli of our four BCC alloys are given in Table 2. Notice that pair correlation function peak widths (see Fig. 2) vary inversely with elastic moduli reported in Table 2; HCP/BCC alloys have the broadest peaks and the lowest moduli. These were obtained by applying a complete set of cell distortions while relaxing the atomic coordinates within the distorted cells, then taking two point central differences. VASP was run on a GPU to accelerate the calculations [19,20]. We employed $3 \times 3 \times 3$ k-point grids and an energy cutoff of 400 eV. Three independent 128-atom configurations were utilized for each value, resulting in 9 independent measures of C_{11} and C_{44} and 18 measures of C_{12} (*i.e.* taking C_{22} and C_{33} as independent values of C_{11}, etc.). Standard deviations of the moduli were 2 GPa or less in every case.

To compare the moduli of HEAs with the individual elements, we present composition-weighted average elastic constants,

$$\overline{C}_{ij} = \sum_\alpha x_\alpha C_{ij}^\alpha, \tag{6}$$

in Table 3 (x_α is the mole fraction of chemical species α). In almost all cases, moduli of the HEA fall up to 20% below the averaged elemental moduli, which we can understand as a reflection of the intrinsic disorder of the HEA. The sole exception is the value of C_{12} for CrMoNbV. Generalizing the Voigt, Reuss and Hill approach, we apply the rule of mixtures to define the isotropic moduli

$$\overline{K}_V = \sum_\alpha x_\alpha K_H^\alpha,\ 1/\overline{K}_R = \sum_\alpha x_\alpha / K_H^\alpha,\ \overline{K}_H = (\overline{K}_V + \overline{K}_R)/2 \tag{7}$$

and similarly for $\overline{G}$. Notice that we are averaging elemental values of Hill moduli, K_H and G_H, because the individual elemental crystalline grains are presumed randomly oriented. We employ $\overline{K}_H$ and $\overline{G}_H$ in Eq. (3) for the Poisson ratio $\overline{\sigma}$, however the anisotropy is taken as $\overline{A}_Z = 2\overline{C}_{44}/(\overline{C}_{11} - \overline{C}_{12})$.

Table 1
Calculated elastic constants of elemental BCC refractory metals (GPa). VRHZ stands for the Voigt-Reus-Hill averages and Zener anisotropy, Eqs. (1)–(4). Stability violations are in bold.

moduli	C_{11}	C_{12}	C_{44}	μ	C_{11}	C_{12}	C_{44}	μ	C_{11}	C_{12}	C_{44}	μ
VRHZ	K_H	G_H	σ	A_Z	K	G	σ	A_Z	K	G	σ	A_Z
element	Ti				V				Cr			
moduli	95	115	41	**−10**	278	143	24	68	444	62	99	191
VRHZ	108	**−10**	**0.55**	**−3.97**	188	37	0.41	0.36	188	129	0.22	0.52
element	Zr				Nb				Mo			
moduli	87	93	34	**−3**	247	137	17	55	469	159	101	155
VRHZ	91	5	0.47	**−10.4**	173	28	0.42	0.31	263	120	0.30	0.65
element	Hf				Ta				W			
moduli	73	116	53	**−22**	268	161	79	54	519	199	141	160
VRHZ	102	**−54**	**0.83**	**−2.50**	197	67	0.35	1.45	306	149	0.29	0.88

Table 2
Elastic moduli (GPa) of BCC refractory HEAs.

moduli	C_{11}	C_{12}	C_{44}	μ	C_{11}	C_{12}	C_{44}	μ
VRHZ	K_H	G_H	σ	A_Z	K_H	G_H	σ	A_Z
alloy	NbTiVZr				CrMoNbV			
moduli	161	103	29	29	354	143	51	105
VRHZ	122	29	0.39	0.99	213	69	0.35	0.48
alloy	HfNbTaZr				MoNbTaW			
moduli	159	108	41	25	371	160	69	106
VRHZ	125	34	0.38	1.63	230	82	0.34	0.65

Table 3
Averaged moduli of BCC refractory elements as defined in the text (Eq. (6) and (7).

moduli	$\overline{C}_{11}$	$\overline{C}_{12}$	$\overline{C}_{44}$	$\overline{\mu}$	$\overline{C}_{11}$	$\overline{C}_{12}$	$\overline{C}_{44}$	$\overline{\mu}$
VRHZ	$\overline{K}_H$	$\overline{G}_H$	$\overline{\sigma}$	$\overline{A}_Z$	$\overline{K}_H$	$\overline{G}_H$	$\overline{\sigma}$	$\overline{A}_Z$
alloy	NbTiVZr				CrMoNbV			
moduli	177	122	29	27	360	125	60	117
VRHZ	134	19	0.43	1.05	201	65	0.35	0.52
alloy	HfNbTaZr				MoNbTaW			
moduli	169	127	45	21	376	164	84	106
VRHZ	133	14	0.45	2.13	229	76	0.35	0.80

3. Atomic displacements

Atoms displace from their ideal lattice sites due to thermal vibrations and random placement of differing sizes. Sometimes referred to as "lattice distortion" [21–23], this effect reflects the interplay of thermal and interatomic forces creating displacements with elastic properties that resist them. It is important because it can provide a mechanism to strengthen the alloy [24,25].

We choose to define the lattice distortion, Λ, as the root-mean-square average of the atomic displacement $\mathbf{u}$ from the ideal lattice sites. This choice is advantageous because provides the isotropic atomic displacement parameter [26], U_{eq} via

$$\Lambda \equiv \sqrt{\left\langle |\mathbf{u}|^2 \right\rangle}, \quad U_{eq} = \frac{1}{3}\Lambda^2. \tag{8}$$

Fig. 3 displays U_{eq} obtained from simulations over a range of temperatures. For each compound, four independent $N = 128$-atom configurations were drawn from MCMD simulations at $T = 1200$ K and relaxed to $T = 0$ K. Each configuration was then equilibrated for several ps at various temperatures using conventional molecular dynamics to preserve the chemical order characteristic of 1200 K. Averages were then taken over an additional 200fs or more of molecular dynamics time, over all 128 atoms, and all four independent configurations. All molecular dynamics simulations utilized VASP with settings as described in Section 2, except we employ a $2 \times 2 \times 2$ k-point grid. MD simulations were performed at the relaxed volumes.

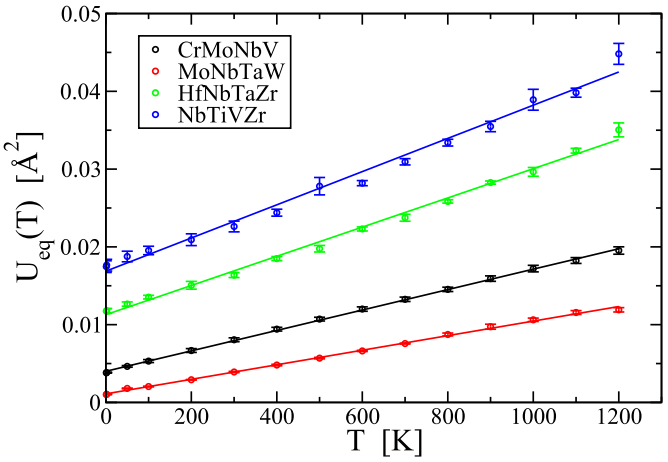

Fig. 3. Isotropic atomic displacement parameter $U_{eq} = \Lambda^2/3$ as defined in Eq. (8), including size effect ($T \to 0$ limit) and thermal displacements (slope).

Thermally excited atomic vibrations generate the dynamical Debye Waller factor that scales diffraction peak intensities as $I(\mathbf{G}) = I_0(\mathbf{G})e^{-2W}$, where $\mathbf{G}$ is a reciprocal lattice vector. In the case of isotropic elasticity, $2W = U_{eq}|\mathbf{G}|^2$ [27]. Random interatomic interactions in our high entropy alloy create an additional static contribution to the lattice distortion that remains even as $T \to 0$. This is known as the size effect [28–30] and its contribution to the Debye-Waller factor and to diffuse scattering were analyzed by Huang [31] in the limit of dilute solutions. According to this theory, the $T = 0$ K lattice distortion Λ_0 should grow proportionally to the variance of atomic size:

$$\sigma_d = \sqrt{\left\langle d^2 \right\rangle - \langle d \rangle^2} \tag{9}$$

Here we define the effective atomic size d_α of species α in the HEA as the peak position of the near-neighbor pair correlation function $g_{\alpha\alpha}(r)$. Lattice distortion and size variance are compared in Table 4. Although Λ varies monotonically with σ_d, they are not directly proportional. This may reflect the complexity of concentrated solid

Table 4
Comparison of $T = 0$ K lattice distortion (Λ_0, units Å) with atomic size variance (σ, Å), and simulated slope of thermal displacements (dU_{eq}/dT, $Å^2/K\times10^{-4}$) with predicted slope ($k_Bk_D/2\pi^2C$, units $Å^2/K\times10^{-4}$).

	Λ_0	σ_d	$\frac{dU_{eq}}{dT}$	$\frac{k_Bk_D}{2\pi^2C}$	Λ_0	σ_d	$\frac{dU_{eq}}{dT}$	$\frac{k_Bk_D}{2\pi^2C}$
alloy	NbTiVZr				CrMoNbV			
	0.225	0.341	0.213	0.259	0.110	0.239	0.131	0.122
alloy	HfNbTaZr				MoNbTaW			
	0.184	0.314	0.188	0.223	0.058	0.173	0.094	0.097

solutions, where correlations in chemical occupation can influence the effective size of individual atoms. For example, an excess of small atoms surrounding a large one may partially cancel the lattice dilation due to the large atom, but an excess of large neighbors could increase it.

Notice in Fig. 2 that the HEAs containing only normal BCC elements exhibit a preference for unlike (LR) neighbors. This means that small atoms preferentially cluster around large, and vice-versa. As a result, the static contributions to the $T = 0$ lattice distortions are partially canceled by correlations, and the atoms remain close to their ideal lattice sites. In contrast, for HEAs containing HCP/BCC elements, there is no such cancellation. Indeed, there is a tendency for Zr atoms to segregate [5]. As a result the static contributions may even be *enhanced* by correlations, and the atoms displace far from their ideal sites.

Thermal contributions to the atomic displacement parameter can be evaluated from the phonon dispersion relation $\omega_s(\mathbf{k})$, where ω is the frequency of a mode of polarization s (*e.g.* longitudinal or transverse) and $\mathbf{k}$ is the phonon wavevector. In the continuum limit at long wavelengths, $\omega_s(\mathbf{k}) = v_sK^2$ where the sound speed $v_s = \sqrt{C_s/\rho}$ with C_s a suitable combination of elastic moduli, and ρ the mass density. For example: $C_s = C_{11}$ or C_{44}, respectively, for longitudinal or transverse sound propagating in the cubic [100] direction; $C_s = (C_{11} + 2C_{12} + 4C_{44})/3$ or $(C_{11} - C_{12} + C_{44})/3$ in the [111] direction; $C_s = (C_{11} + C_{12} + 2C_{44})/2$, $(C_{11} - C_{12})/2$, or C_{44} in the [110] direction [27].

Applying the law of equipartition for classical harmonic vibrations, we have

$$U_{eq} = \frac{N}{3}\sum_s \int \frac{d\mathbf{k}}{V_{BZ}} \frac{k_BT}{\rho V\omega_s^2(\mathbf{k})} \tag{10}$$

where N is the total number of atoms in volume V. We evaluate Eq. (10) by assuming a Debye density of states with isotropic sound speeds, relating the Brillouin zone volume V_{BZ} to the BCC lattice constant a, and dropping factors of order 1, to obtain

$$U_{eq} = \frac{k_BT}{2\pi^2C}k_D, \quad k_D = \sqrt[3]{6\pi^2N/V}. \tag{11}$$

The elastic constant C is defined as an average over orientations and polarizations *via*.

$$\frac{3}{C} \equiv \sum_s \int \frac{d\hat{\mathbf{k}}}{4\pi} \frac{1}{C_s\left(\hat{\mathbf{k}}\right)}. \tag{12}$$

In practice we shall evaluate C through a multiplicity-weighted sum over 2-fold, 3-fold and 4-fold symmetry directions.

Provided we remain in the harmonic approximation assumed in Eq. (10), the thermal contribution to U_{eq} should simply add to the contribution from the size effect [31], leading to linear variation with respect to temperature T. Table 4 tests our prediction (Eq. (11)) and shows that the thermal displacements agree pretty well with respect to our theoretical prediction. Comparing dU_{eq}/dT to $k_Bk_D/2\pi^2C$ among the four compounds, we find these values agree to within 20%.

4. Conclusions

In conclusion, we demonstrate that inclusion of BCC/HCP elements in refractory HEAs reduces the shear modulus $\mu = (C_{11} - C_{12})/2$. Indeed, a tetragonal distortion has been reported in the Zr-rich regions of phase segregated BCC/HCP containing HEAs [5]. This effect may be related to the elastic instability of the BCC/HCP elements arising from the Fermi level lying in a peak of the electronic density of states. Although inclusion of regular BCC elements stabilizes the BCC HEA, it should be possible to drive the system close to a shear instability by increasing the BCC/HCP content, and thereby achieving a high Poisson ratio and potentially enhancing ductility. Examples of compositions predicted to be on the threshold of low temperature instability based on the averaged elemental modulus $\bar{\mu}$ are $Nb_{0.06}$ $Ti_{0.63}$ $V_{0.06}$ $Zr_{0.25}$ and $Hf_{0.53}$ $Ta_{0.11}$ $Nb_{0.11}$ $Zr_{0.25}$.

We quantified the $T = 0$ K lattice distortion Λ_0 and demonstrated growth of $\Lambda(T)$ at $T > 0$ is governed by the inverse elastic moduli. At $T = 0$ we find that the atomic size effect contributes to lattice distortion as predicted by Huang [31], but we found evidence for other effects associated with interatomic correlations that may either diminish or enhance distortion depending on whether large and small atoms attract or repel. Engineering alloys to alter interatomic interactions or to reduce shear moduli can thus enhance lattice distortion and thereby potentially increase hardness relative to undistorted structures with similar elastic moduli.

Acknowledgement

This work was supported by the Department of Energy under grant DE-SC0014506 and by the Pittsburgh Supercomputer Center under XSEDE grant DMR160149. We acknowledge useful discussions with Michael Gao and Takeshi Egami.

References

[1] B. Cantor, I.T.H. Chang, P. Knight, A.J.B. Vincent, Microstructural development in equiatomic multicomponent alloys, Mat. Sci. Eng. A 375–77 (2004) 213–218.
[2] J.-W. Yeh, S.-K. Chen, S.-J. Lin, J.-Y. Gan, T.-S. Chin, T.-T. Shun, C.-H. Tsau, S.-Y. Chang, Nanostructured high-entropy alloys with multiple principal elements: novel alloy design concepts and outcomes, Adv. Eng. Mater. 6 (2004) 299–303.
[3] O.N. Senkov, G.B. Wilks, D.B. Miracle, C.P. Chuang, P.K. Liaw, Refractory high-entropy alloys, Intermetallics 18 (2010) 1758–1765.
[4] O. Senkov, J. Scott, S. Senkova, D. Miracle, C. Woodward, Microstructure and room temperature properties of a high-entropy TaNbHfZrTi alloy, J. Alloys Compd. 509 (2011) 6043–6048.
[5] S. Maiti, W. Steurer, Structural-disorder and its effect on mechanical properties in single-phase TaNbHfZr high-entropy alloy, Acta Mater. 106 (2016) 87–97.
[6] W. Burgers, On the process of transition of the cubic-body-centered modification into the hexagonal-close-packed modification of zirconium, Physica 1 (1934) 561–586.
[7] K. Masuda-Jindo, S.R. Nishitani, V. Van Hung, HCP-BCC structural phase transformation of titanium: analytic model calculations, Phys. Rev. B 70 (2004) 184122.
[8] M. Born, On the stability of crystal lattices. I, Math. Proc. Camb. Phil. Soc. 36 (1940) 160–172.
[9] M. Widom, Entropy and diffuse scattering: comparison of NbTiVZr and CrMoNbV, Met. Mat. Trans. A 47 (2016) 3306–3311.
[10] M. Widom, W. Huhn, S. Maiti, W. Steurer, Hybrid monte carlo/molecular dynamics simulation of a refractory metal high entropy alloy, Met. Mat. Trans. A 45 (2014) 196–200.
[11] W. Guo, W. Dmowski, J.-Y. Noh, P. Rack, P.K. Liaw, T. Egami, Local atomic structure of a high-entropy alloy: an x-ray and neutron scattering study, Met. Mat. Trans. A 44 (2013) 1994–1997.

[12] G. Kresse, D. Joubert, From ultrasoft pseudopotentials to the projector augmented-wave method, Phys. Rev. B 59 (1999) 1758–1775.
[13] J.P. Perdew, K. Burke, M. Ernzerhof, Generalized gradient approximation made simple, Phys. Rev. Lett. 77 (1996) 3865–3868.
[14] R. Hill, The elastic behaviour of a crystalline aggregate, Proc. Phys. Soc. A 65 (1952) 349–354.
[15] W. Voigt, Lehrbuch der Kristallphysik, 1928. Teubner, Leipzig.
[16] A. Reuss, Berechnung der fliessgrenze von mischkristallen auf grund der plastizittsbedingung fur einkristalle, Z. Angew. Math. Mech. 9 (1929) 49–58.
[17] M. de Jong, W. Chen, T. Angsten, A. Jain, R. Notestine, A. Gamst, M. Sluiter, C.K. Ande, S. van der Zwaag, J.J. Plata, C. Toher, S. Curtarolo, G. Ceder, K.A. Persson, M. Asta, Charting the complete elastic properties of inorganic crystalline compounds, Sci. Data 2 (2015) 150009.
[18] C. Zener, Contributions to the theory of beta-phase alloys, Phys. Rev. 71 (1947) 846–851.
[19] M. Hutchinson, M. Widom, VASP on a GPU: application to exact-exchange calculations of the stability of elemental boron, Comput. Phys. Commun. 183 (2012) 1422–1426.
[20] M. Hacene, A. Anciaux-Sedrakian, X. Rozanska, D. Klahr, T. Guignon, P. Fleurat-Lessard, Accelerating VASP electronic structure calculations using graphic processing units, J. Comp. Chem. 33 (2012) 2581–2589.
[21] W. Rosenhain, Solid solutions, Trans. Amer. Inst. Min. Met. Eng. 69 (1923) 1003.
[22] W.G. Burgers, F.J. Lebbink, Lattice distortions and shear in aluminium single crystals, Nature 157 (1946), 47–47.
[23] J.W. Yeh, Recent progress in high-entropy alloys, Ann. Chim. Sci. Mater 31 (2006) 633–648.
[24] C. Varvenne, A. Luque, W.A. Curtin, Theory of strengthening in fcc high entropy alloys, Acta Mat. 118 (2016) 164–176.
[25] H.S. Oh, D. Ma, G.P. Leyson, B. Grabowski, E.S. Park, F. Kormann, D. Raabe, Lattice distortions in the FeCoNiCrMn high entropy alloy studied by theory and experiment, Entropy 18 (2016) 321.
[26] K.N. Trueblood, H.-B. Bürgi, H. Burzlaff, J.D. Dunitz, C.M. Gramaccioli, H.H. Schulz, U. Shmueli, S.C. Abrahams, Atomic displacement parameter nomenclature. Report of a subcommittee on atomic displacement parameter nomenclature, Acta Cryst. A 52 (1996) 770–781.
[27] C. Kittel, Introduction to Solid State Physics, eighth ed., Wiley, 2005.
[28] M.A. Krivoglaz, X-ray and Neutron Diffraction in Nonideal Crystals, Springer, Berlin, 1996.
[29] W. Schweika, Disordered Alloys: Diffuse Scattering and Monte Carlo Simulations, in: Tracts in Modern Physics, vol. 141, Springer, 1998.
[30] T.R. Welberry, Diffuse X-Ray Scattering and Models of Disorder, in: IUCR Monographs on Crystallography, vol. 16, 2004. Oxford.
[31] K. Huang, X-ray reflexions from dilute solid solutions, Proc. Roy. Soc. Lond. A 190 (1947) 102–117.